Joule

Article

# Harnessing triboiontronic Maxwell's demon by triboelectric-induced polarization for efficient energy-information flow

## Graphical abstract

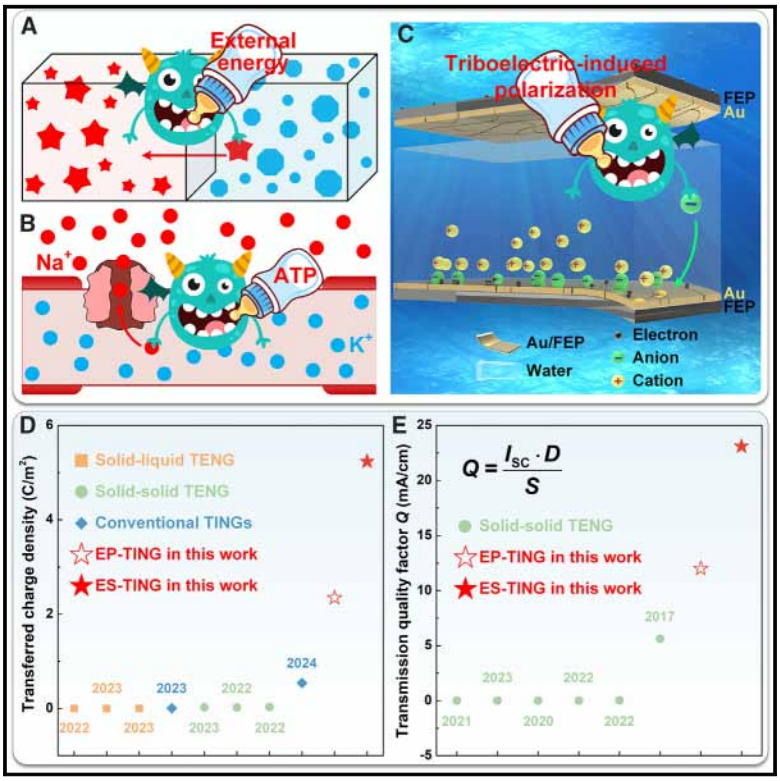


## Highlights

- Triboiontronic Maxwell's demon was realized by triboelectric-induced polarization
- An EP-TING achieved a transferred charge density of 2,347.12 mC/m$^2$
- An ES-TING achieved a transferred charge density of 5,237.51 mC/m$^2$
- Bionic neural circuits enabled interference-resistant underwater transmission


## Authors

Xiang Li, Yu Wei, Xiang Gao, Zhongqiang Zhang, Zhong Lin Wang, Di Wei

## Correspondence

dw344@cam.ac.uk



## In brief

Inspired by nerve transmission, triboiontronic Maxwell's demon was established through triboelectric-induced polarization of electrostatic fields, enabling remote regulation of charge distribution and migration within electrical double layers (EDLs) and fine-tuning of metal work functions. Our work shows energy generation inherently constitutes a stream of information, and harnessing triboiontronic Maxwell's demon provides an efficient energy-information flow, proving crucial in the post-Moore era.


Li et al., 2025, Joule 9, 101888
May 21, 2025 
https://doi.org/10.1016/j.joule.2025.101888

CellPress

Joule

CellPress

Article

# Harnessing triboiontronic Maxwell's demon by triboelectric-induced polarization for efficient energy-information flow

Xiang Li,[1,2] Yu Wei,[1,2] Xiang Gao,[3] Zhongqiang Zhang,[3] Zhong Lin Wang,[1] and Di Wei[1,4,5,*]
[1]Beijing Institute of Nanoenergy and Nanosystems, Chinese Academy of Sciences, Beijing 101400, P.R. China
[2]School of Nanoscience and Engineering, University of Chinese Academy of Sciences, Beijing 100049, P.R. China
[3]School of Mechanical Engineering, Jiangsu University, Zhenjiang 212013, P.R. China
[4]Centre for Photonic Devices and Sensors, University of Cambridge, 9 JJ Thomson Avenue, Cambridge CB3 0FA, UK
[5]Lead contact
*Correspondence: dw344@cam.ac.uk
https://doi.org/10.1016/j.joule.2025.101888

**CONTEXT & SCALE** Maxwell's demon presents an apparent challenge to the second law of thermodynamics by selectively sorting molecules to reduce entropy and create a gradient. Over time, Maxwell's demon analogs have evolved into molecular processors, pumps, and ratchets powered by light or external fields. In neural transmission, $Na^+$ ions generate action potentials that efficiently convey information while simultaneously restoring salinity gradients—a process that mirrors the demon's selective sorting and highlights the intrinsic link between energy and information. Achieving this seamless energy-information transfer, as seen in neurotransmission, remains a substantial challenge. In this study, triboiontronic Maxwell's demon was realized through triboelectric-induced polarization of electrostatic fields, enabling remote control over charge distribution and migration within electrical double layers (EDLs) and allowing for precise tuning of metal work functions. This approach underscores a promising pathway toward integrating energy-information flow in advanced systems.

## SUMMARY

Maxwell's demon seemingly violates the second law of thermodynamics, but in reality, it requires external energy for information processing and particle control, thereby ensuring an overall increase in system entropy. Here, triboiontronic Maxwell's demon was established by triboelectric-induced polarization, enabling remote regulation of charge migration within electrical double layers (EDLs). For energy flow, an enhanced physical-adsorption triboiontronic nanogenerator (EP-TING) achieved a remarkable transferred charge density of 2,347.12 $mC/m^2$, surpassing conventional EDL-based technologies by several orders of magnitude. Furthermore, the advanced synergy-enhanced strategy TING (ES-TING), integrating redox reactions, further increased the charge density to 5,237.51 $mC/m^2$, marking a significant breakthrough in energy conversion efficiency. For information flow, bionic neural circuits utilizing EP-TINGs/ES-TINGs enabled highly portable, interference-resistant underwater transmission systems with minimal energy consumption, effectively addressing challenges of acoustic multipath interference, environmental noise, and severe signal attenuation. Therefore, harnessing triboiontronic Maxwell's demon provides an efficient energy-information flow, proving crucial in the post-Moore era.

## INTRODUCTION

Maxwell's demon, a thought experiment proposed by physicist James Clerk Maxwell in the 19th century,[1] appears to challenge the second law of thermodynamics. The demon is imagined to selectively separate molecules to reduce the system's overall entropy, creating a gradient that represents a potential energy source.[2] This notion raised a profound question: can entropy be reduced without consuming energy? Maxwell's demon sparked significant debate in the scientific community, leading to deeper investigations into the relationship between information, entropy, and energy and contributing to the development of information theory.[3,4] On the macroscopic level, it appears to violate the second law of thermodynamics, as the demon

selectively allows fast-moving molecules to pass through a gate, seemingly separating hot and cold regions and decreasing the system's entropy. However, this process requires the consumption of external energy for the demon to perform tasks such as observation and control of the molecules.[5] This energy expenditure ensures that the overall entropy of the system still increases, following the second law. On the microscopic level, the demon's operation involves molecular motion and information processing, which requires energy for the acquisition and manipulation of information.[6,7] The process of obtaining and processing this information itself consumes energy, which leads to an increase in the system's entropy, aligning with the second law as well. Both aspects of understanding highlight that energy flow is intrinsically linked to information processing. It was demonstrated that the demon must expend energy as a thermodynamic cost to acquire information about molecules to achieve control of molecular dynamics (MD), thereby restoring compliance with the second law when considered as part of the entire system. Analogous to precise molecular regulation, Maxwell's demon analogs driven by external fields, such as light, have been achieved at the microscopic nanoscale.[8,9] For instance, the demon, a microwave cavity, encodes quantum information from a superconducting qubit and converts it into work by amplifying a propagating microwave pulse via stimulated emission.[10] In the meanwhile, a light-driven molecular pump demon used wavelength-specific information to induce reversible structural changes in a compound for creating a proton concentration gradient, which could generate electrical current with ~0.12% efficiency.[11] Despite these molecular-scale successes and advances in light-driven Maxwell's demons facilitating directional compound transport over centimeter-scale distances,[12] efficiently coupling energy and information flow at the macroscopic level remains a significant challenge.

In neural transmission,[13] the generation of action potentials is driven by shifts in ion distribution across the neuronal membrane. In the resting state, the intracellular environment contains a high concentration of $K^+$ ions, while the extracellular space is rich in $Na^+$ ions, establishing the resting membrane potential. Upon receiving a stimulus, sodium channels rapidly open, allowing $Na^+$ to flow into the cell, depolarizing the membrane, and triggering an action potential.[14,15] This process disrupts the ion balance across the cell membrane. In the meanwhile, the sodium-potassium pump as an ion pump consumes adenosine triphosphate (ATP) to actively transport $Na^+$ and $K^+$ against their concentration gradients to restore the salinity gradient and membrane resting potential,[16,17] ensuring rapid and efficient signal transmission. Functioning like a biological Maxwell's demon, the sodium-potassium pump actively restores salinity gradients across the neuronal membrane, facilitating the efficient conversion of energy into information and supporting the neural system's high efficiency. Thus, neural signal transmission exemplifies the efficient conversion of energy into information, illustrating the principle that energy generation inherently constitutes a stream of information. This principle underscores the extraordinary efficiency of the human brain, which, despite containing tens of billions of neurons, operates on merely 12 W of power,[18] surpassing the efficiency of any artificial system designed to emulate its functions.

Unlike macroscopic ion transport behavior, the ion transport process in the nanoconfined space of biological systems could be regulated.[19–21] Such special ion dynamics is due to the different ion interactions within different confined space limits. In nanoconfined spaces, a range of anomalous ionic behaviors such as electrical double layer (EDL) overlapping, ionic Coulomb blockade, superionic states, etc. will appear.[22,23] This provides an opportunity to biomimic ionic flows in neural transmission processes by the nanoconfined iontronics that use ions as charge carriers.[24,25] In contrast to conventional electronics, which depend solely on electron transfer driven by electric fields, iontronics employs multiphysical fields to generate ion concentration gradients, allowing for the efficient use of ions with varying valence states as charge carriers.[26,27] The foundation of iontronics lies in the EDL at the solid-liquid interface, where ionic-electronic interactions occur within its nanometer thickness.[24,28] The key challenge is to control ion migration and enhance ionic-electronic coupling at the EDL for efficient energy and information transfer. Inspired by biological Maxwell's demon in neural transmission that consumed ATP to drive the inverse gradient migration of ions to maintain a stable concentration gradient, iontronics offers the possibility to emulate Maxwell's demon by fine-tuning the nanoconfined EDL with external fields to regulate ion migration and achieve efficient energy-information flow. Success in this area could significantly enhance energy conversion and information transfer, advancing next-generation technologies and biological system simulations.

In this study, a triboiontronic Maxwell's demon was developed through triboelectric-induced polarization of electrostatic fields, enabling remote control of charge distribution and migration within EDLs, thereby promoting asymmetric EDL formation and optimizing energy and information flow. An efficient triboelectric-induced polarization strategy was developed using a hybrid material composed of a dielectric coated with an ultrathin metal layer. This strategy forms the foundation for all EDL regulation, allowing precise control over charge distribution and migration. By adjusting the dielectric's electronegativity, solid-liquid contact electrification (CE) was modulated, while the ultrathin metal layer enabled triboelectric effects to influence surface charge behavior within the EDL. The developed triboiontronic Maxwell's demon enabled effective control over EDL charge dynamics, significantly enhancing ionic-electronic coupling and establishing the EDL as a tailored interface for triboiontronic applications. In terms of energy flow, this triboiontronic Maxwell's demon facilitated the development of an enhanced physical-adsorption triboiontronic nanogenerator (EP-TING), which achieved controlled ion migration with a transferred charge density of 2,347.12 $mC/m^2$, substantially higher than conventional triboelectric nanogenerators (TENGs) and other EDL-based energy harvesters. An advanced enhanced synergy-strategy TING (ES-TING), incorporating redox reactions, further increased ion mobility, boosting the transferred charge density to 5,237.51 $mC/m^2$, representing a significant advancement in energy generation. For information flow, bionic neural circuits based on EP-TINGs or ES-TINGs facilitated advanced remote wireless underwater transmission with a quality factor surpassing conventional TENGs. This configuration provided a compact, interference-resistant underwater communication system with

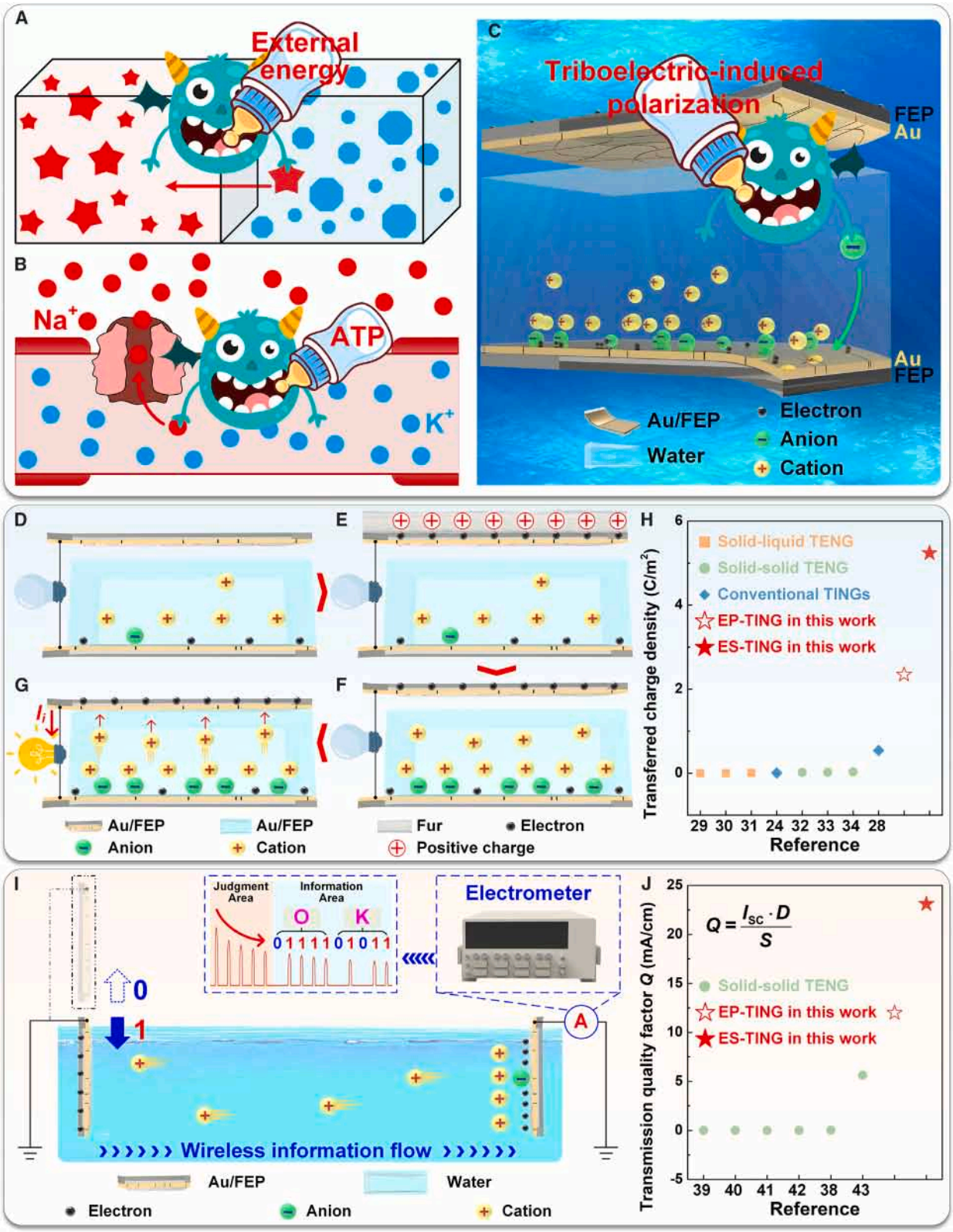


*(legend on next page)*

minimal energy consumption, effectively overcoming major challenges in underwater communication such as acoustic multipath interference, optical absorption, and electromagnetic attenuation. In the context of bionic neural signal transmission, energy generation, akin to action potentials, inherently carries information. By adjusting ion types or concentrations within EP-TINGs or ES-TINGs, the polarity of charge carriers can be precisely managed, directing current flow and forming a flexible, energy-independent platform for human-machine interfaces and logical control. Furthermore, triboelectric-induced polarization in the solid-solid triboelectric charging of the dielectric back layer enabled tunable control over the work function of the top metal layer. This tunability is crucial for optimizing broader energy-harvesting technologies, such as perovskite and other solar cells, as it directly affects energy level alignment, charge extraction, and device efficiency. In conclusion, triboelectric-induced polarization provides a versatile mechanism to emulate Maxwell's demon, creating and regulating concentration gradients and allowing remote control over EDL charge distribution across diverse dielectrics. In addition, it was demonstrated how modifying charge distribution within the nanoscale EDL could directly influence the macroscopic performance of the device. This mechanism not only facilitates efficient energy-information flow, vital in the post-Moore era, but also advances energy-efficient neuromorphic computing and integrated sensing-computation systems.

## RESULTS AND DISCUSSION

### Triboiontronic Maxwell's demon created by triboelectric-induced polarization

Maxwell's demon appears to violate the second law of thermodynamics but ultimately requires external energy to regulate entropy reduction within the system. The classical demon controls a gate between compartments, seemingly decreasing entropy and creating order without energy expenditure (Figure 1A). However, the demon must process information about particle movement and determine when to open the gate, an action that necessitates energy. The entropy increase associated with the demon's memory and decision-making offsets the entropy reduction from particle sorting. Consequently, the total entropy of the system, including the demon, continues to increase, preserving the second law. A similar principle governs neural signal transmission. Upon stimulation, $Na^+$ migrate along their concentration gradient, generating action potentials that seemingly enable efficient information transfer without direct energy input. However, the $Na^+$ pump functions as a biological Maxwell's demon, utilizing ATP to actively transport $Na^+$ against its concentration gradient, restoring ion balance and membrane resting potential (Figure 1B). This process ensures a sustained concentration gradient, enabling rapid and efficient signal propagation in subsequent action potentials. Inspired by the biological Maxwell's demon in neural signal transmission, a triboiontronic Maxwell's demon was demonstrated, where triboelectric-induced polarization enhanced the formation of the asymmetric EDLs, enabling efficient energy-information flow. By consuming mechanical energy during solid-solid CE, this mechanism reinforced ion concentration gradients, further amplifying the asymmetry in the formation of EDLs. Specifically, in terms of energy generation, employing triboiontronic Maxwell's demon, an enhanced EP-TING was developed (Figure 1C), which could achieve ultra-high transferred charge density. In the EP-TING, the ultrathin metal layer with a thickness of tens of nanometers was sputtered on the dielectric substrate via magnetron deposition in the hybrid film, and approximately 200 μL of water was initially dropped onto the bottom hybrid film (e.g., gold/fluorinated ethylene propylene, Au/FEP). Water infiltrated microscopic cracks in the Au layer, directly contacting the more electronegative FEP substrate and forming the bottom EDL (Figure 1D). At this time, the surface electrostatic potential of the FEP substrate surface in the top Au/FEP layer was approximately 0 V. Then, the FEP substrate in the top Au/FEP film, isolated from the liquid, was rubbed by electropositive fur, inducing solid-solid CE through mechanical energy consumption (Figure 1E). Upon removal of the fur (Figure 1F), a large number of electrons remained on the FEP surface, and the surface electrostatic potential of the FEP substrate was measured to be approximately −2,600 V. This change indicated the generation of the triboiontronic Maxwell's demon via triboelectric-induced polarization. The resulting electrostatic field remotely drove anions toward the bottom solid-liquid interface and cations in the opposite direction, counter to their concentration gradients, thereby increasing the charge density within the bottom EDL. Subsequently, the Au surface in the top Au/FEP layer was pressed downward, initiating contact with the water and forming the top EDL. Through the action of the triboiontronic Maxwell's demon, an enhanced formation of asymmetric EDLs occurred, leading to a stronger concentration gradient that effectively controlled the migration of cations within the EP-TING (Figure 1G). The ultrathin Au layer not only ensured that triboelectric effects remotely influenced the surface charge distribution within the EDL but also served as a charge-collecting layer, facilitating the conversion of ion migration into electron transfer within the external circuit. This ultimately enabled the conversion of triboelectric energy into electrical energy. Through repeated contact and separation cycles, the ion concentration gradient within the asymmetric EDLs progressively diminished, leading to a gradual reduction in electrical output that continued until equilibrium was

**Figure 1. Triboiontronic Maxwell's demon, created by triboelectric-induced polarization, could realize efficient energy-information flow**

(A) Maxwell's demon requires an external energy input to process molecular information and exert control over molecular behavior.

(B) The $Na^+$ ion pump as biological Maxwell's demon could efficiently convert ATP to actively transport ions against their concentration gradients.

(C) Employing triboiontronic Maxwell's demon, the EP-TING was developed.

(D–G) The working principle of triboiontronic Maxwell's demon in the EP-TING.

(H) Comparison of the transferred charge density of typical different types of generators.

(I) The operating principle of the bionic neurologic circuit via the EP-TING to realize wireless information transmission.

(J) The transmission quality factor Q comparison of different types of means for wireless information transmission underwater.

reached between the two EDLs. Through adjustment of the ions' charge-carrying capacity (i.e., different concentrations or valences of ions), the EP-TING achieved an impressive transferred charge density of 2,347.12 mC/m$^2$ (Figure 1H). Moreover, by varying the types of metal layers on dielectric substrates via magnetron sputtering, redox reactions could be introduced into the EP-TING, resulting in the more advanced ES-TING (Note S1; Figure S1). It synergized with the enhanced asymmetric EDLs to promote more efficient and stable ion migration, achieving a transferred charge density of up to 5,237.51 mC/m$^2$ (Figure 1H). Compared with conventional TENGs,[29–34] TINGs,[24,28] and other EDL-regulated energy-harvesting technologies,[35–37] the transferred charge density in the EP-TING and ES-TING was increased by several orders of magnitude, significantly enhancing energy generation capabilities.

In terms of information transmission, akin to the extended propagation of neural signals over several tens of centimeters, optimizing the effective range of the triboiontronic Maxwell's demon within EP-TING could enable highly efficient remote ion migration. This opened the gate to developing a bionic neurological circuit with the capability for advanced remote wireless transmission in water media. Underwater communication technologies encounter fundamental challenges[38]: electromagnetic waves are quickly absorbed by water, optical waves are susceptible to ambient light interference, and acoustic communication, despite widespread use, suffers from multipath interference and Doppler shifts. Conventional TENGs, which generate electrostatic fields through CE to drive electronic displacement or ionic currents, offer potential solutions to these challenges. However, TENGs are constrained by large operational areas and low signal amplitudes, resulting in limited portability and suboptimal signal-to-noise ratios. These issues necessitate further refinement to enhance performance and efficiency. In the bionic neurological circuit via the EP-TING (Figure 1I), the right Au/FEP hybrid film remained immersed in the liquid, maintaining a stable EDL essential for continuous ionic-electronic interactions. By contrast, the left Au/FEP hybrid film, which carried a strong electrostatic field due to pre-established solid-solid CE, was mechanically actuated to periodically contact and separate from the liquid interface according to a predefined actuation protocol. The triboiontronic Maxwell's demon, induced through triboelectric polarization, further enhanced the asymmetry between the EDLs, effectively establishing a robust ion concentration gradient. The asymmetric EDLs significantly expanded the effective range of ionic-electronic coupling beyond the nanoscale of the EDL itself and even extended it several orders of magnitude higher than that achieved by a single EDL, reaching tens of centimeters. So, the ion concentration gradient between the asymmetric EDLs acted as a driving force for directed ion migration, mimicking the synaptic transmission processes observed in biological neural networks. Consequently, the mechanical movement of the left Au/FEP hybrid film was efficiently transduced into precisely controlled electrical pulses, demonstrating the potential of EP-TING in neuromorphic systems and artificial synaptic devices. These pulses were collected by an electrometer and converted into readable character information using the American Standard Code for Information Interchange (ASCII) system (Figure S2). This process enabled the remote transmission and conversion of mechanically encoded physical contact information into corresponding electrical signals. To mitigate information distortion caused by chaotic environmental noise, the ion concentration gradient created by enhanced asymmetric EDLs was gradually reduced over time. The initial five electrical pulses were designated as the "judgment area" to identify the information source, and the subsequent pulses were used to transmit the information. They were classified as the "information area" to ensure accurate information recognition. As a demonstration, the electrical pulses generated by the corresponding mechanical actions successfully conveyed the character information of "OK" via the ASCII system. To accurately assess the transmission quality of wireless information systems, the quality factor $Q$ (unit: A/m) was introduced:

$$Q = \frac{I_{SC} \cdot D}{S} \qquad \text{(Equation 1)}$$

where $I_{SC}$ is the short-circuit current ($I_{SC}$, unit: A), $D$ is the transmission distance (unit: m), and $S$ is the working area of the device (unit: m$^2$). The $Q$ value of the bionic neurologic circuit via the EP-TING reached 12.0 A/m (Figure 1J). Therefore, a higher $Q$ value may indicate stronger signal transmission, an extended communication range, and enhanced portability (smaller working area of the device). By incorporating redox reactions into the ES-TING, the ion concentration gradient was synergistically enhanced (Note S2; Figure S3), significantly increasing it to 23.1 A/m. In comparison, the highest $Q$ value of conventional TENGs for wireless information transmission was up to about 5 A/m.[38–43] This ion concentration gradient drove directed ion migration, mirroring synaptic transmission in biological neural networks. This system demonstrated near-zero energy consumption while maintaining excellent portability, achieved by minimizing the working area (1 cm$^2$) required for effective operation. More importantly, though the thickness of a single EDL was typically on the nanometer scale, both the EP-TING and ES-TING involved the dynamic interaction between two asymmetric EDLs. The regulation of asymmetric EDLs at the nanoscale significantly extended the effective range of ionic-electronic coupling across macroscopic distances, exceeding the confinement of individual EDLs by several orders of magnitude and reaching tens of centimeters. It was demonstrated how modifying charge distribution within the nanoscale EDL could directly influence the macroscopic performance of the device.

## Adjustment of EDL charge distribution by triboelectric-induced polarization

The foundation of iontronics lies in the EDL at the solid-liquid interface. To develop an efficient EP-TING, it is crucial to precisely optimize and adjust the EDL to enhance the ion concentration gradient and facilitate ion migration. Initially, to explore the remotely dynamic regulation of triboelectric-induced polarization on charge distribution within the EDL, measurements were taken of the triboelectric charge carried by the diffuse layer in the liquid and the surface electrostatic potential of the Stern layer. These measurements provided insights into the trends in charge distribution within the EDL. Water droplets

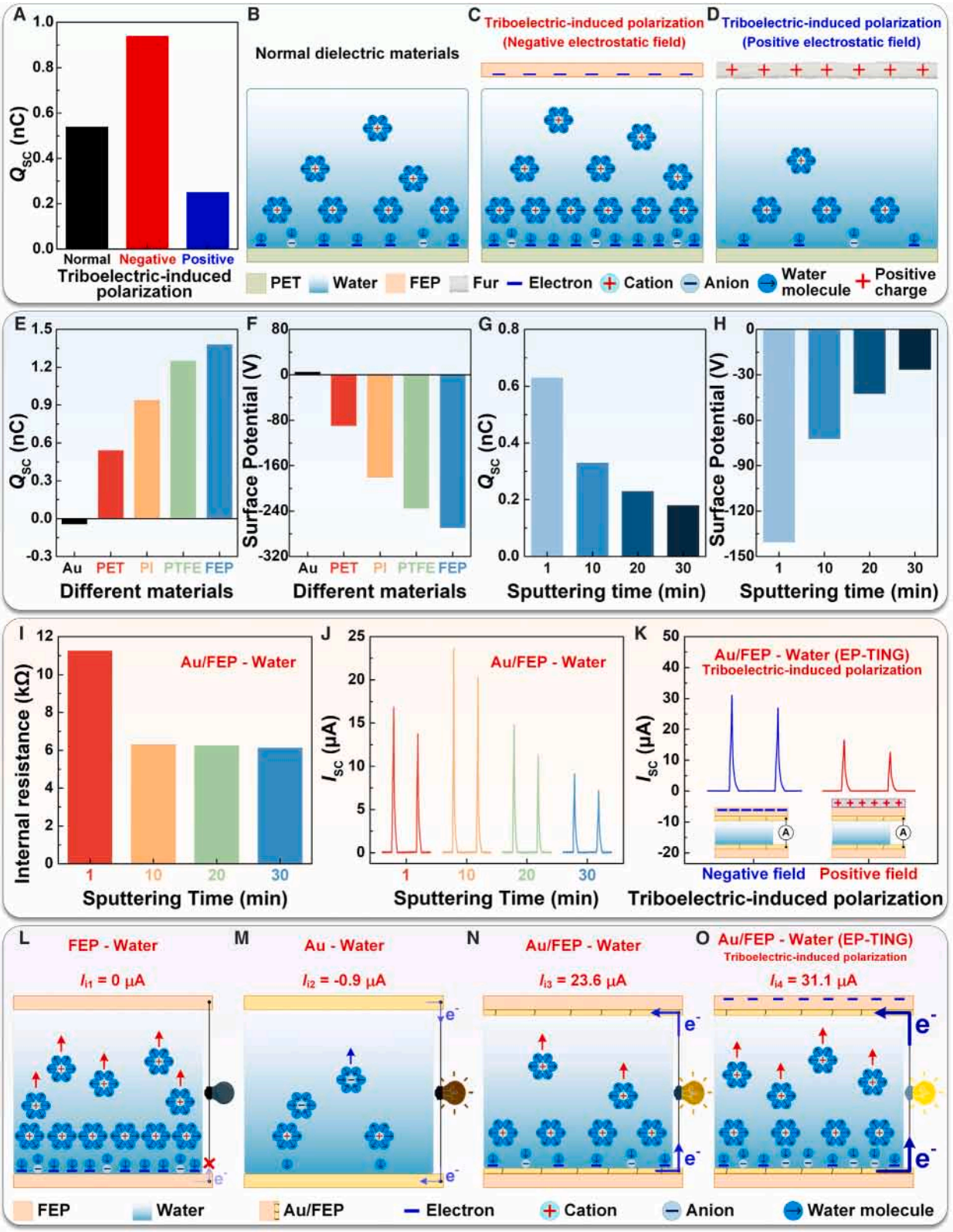


*(legend on next page)*

of approximately 35 μL were deposited on an inclined dielectric film. After sliding about 10 cm along the surface to form an EDL, the droplets were collected using a Faraday cylinder to measure the polarity and amount of triboelectric charge in the diffuse layer (Figure S4). The surface electrostatic potential of the Stern layer on the dielectric film was then assessed with a high-speed surface potentiometer (Figure S5). When the water droplet moved across a polyethylene terephthalate (PET) surface, it carried a positive triboelectric charge of 0.54 nC (Figures 2A and S6), and the PET surface's electrostatic potential was −90 V (Figure S7). When an FEP film, pre-negative-charged through solid-solid CE with fur, was introduced 1 cm on top of the PET film above the water droplet, the triboelectric charge carried by the droplet sliding through the PET surface increased to 0.94 nC, and the surface electrostatic potential increased to −150 V. By contrast, introducing pre-positive-charged fur at the same height reduced the triboelectric charge to 0.25 nC and the surface electrostatic potential to −47 V. This demonstrated that triboelectric-induced polarization, acting as triboiontronic Maxwell's demon, could remotely adjust the charge distribution in the EDL through the electrostatic field. According to the two-step EDL model,[44,45] when water contacted the PET film (Figure 2B), electrons and anions first adsorbed onto the solid surface to form the Inner Helmholtz Plane (IHP). Subsequently, the majority of cations non-specifically adsorbed onto the charged solid surface to form the Outer Helmholtz Plane (OHP), together creating the Stern layer. A minority of cations remained free near the Stern layer, contributing to the formation of the diffuse layer within the droplet. Upon applying a negative electrostatic field above the EDL through pre-CE, a triboiontronic Maxwell's demon was generated via triboelectric-induced polarization. This demon utilized triboelectric energy to remotely drive anions toward the solid-liquid contact interface and cations in the opposite direction, effectively enhancing the charge density within the EDL by further building up their concentration gradients (Figure 2C). Conversely, when a positive electrostatic field was applied at the same position, the reverse regulation of triboelectric-induced polarization was reflected, which drove ions to migrate along their concentration gradient, thereby decreasing the charge density within the EDL (Figure 2D). Secondly, the effects of dielectric substrate electronegativity and ultrathin metal layer coverage on EDL charge density were investigated. Compared with the minimal negative triboelectric charge of −0.05 nC carried by droplets sliding over a pure Au surface (Figures 2E and S8), the positive charge increased progressively from 0.54 to 1.38 nC as droplets passed over PET, polyimide (PI), polytetrafluoroethylene (PTFE), and FEP substrates, respectively. After the droplets had slid off, the positive surface electrostatic potential of the Au remained approximately 5 V (Figures 2F and S9), while the negative surface electrostatic potential of these dielectric films rose from about −90 V to −270 V. This demonstrated that the charge density in the EDL at the metal-liquid interface was lower and oppositely distributed compared with that at the dielectric-liquid interface. Moreover, as the electronegativity of the dielectric film increased, its solid-liquid CE with water intensified, resulting in a higher charge density in the EDL. When FEP with higher electronegativity was used as the dielectric substrate, increasing the Au layer sputtering time from 1 to 30 min reduced the positive triboelectric charge carried by droplets sliding on the Au/FEP hybrid film from 0.63 to 0.18 nC (Figures 2G and S10), while the negative electrostatic potential on these Au/FEP hybrid films decreased from −141 V to −27 V (Figures 2H and S11). This suggested that prolonged sputtering, which enhanced the coverage of the ultrathin metal layer, minimized microscopic cracks (Figure S12) that otherwise facilitated direct contact between the dielectric substrate and the liquid, thereby weakening CE and reducing the charge density in the EDL.

The ultrathin metal layer not only facilitated solid-liquid CE in modulating surface charge distribution within the EDL but also played a crucial role in charge collection due to their higher electrical conductivity. However, an excessively thin metal layer could compromise conductivity, increase internal resistance, and weaken the coupling dynamics between ion migration and electron transfer. Thus, optimizing the sputtering time was essential to achieving a balanced performance. As shown in Figure 2I, increasing the sputtering time of the Au layer from 1 to 10 min effectively reduced the internal resistance of the device from 11.3 to 6.3 kΩ. Beyond this point, a further increase in sputtering time resulted in minimal reduction, and it stabilized around 6.0 kΩ. In addition, if the sputtering time was further increased, the metal layer would be too thick, weakening the CE effect between the liquid and the dielectric substrate. Thus, the optimization of the sputtering time to 10 min resulted in optimal performance for the conventional TING without the influence of triboelectric-induced polarization, resulting in a positive $I_{SC}$ of 23.57 μA and a $Q_{SC}$ of 1.20 μC (Figures 2J and S13). Once the FEP surface in the top Au/FEP hybrid film was rubbed with the electropositive fur, the triboiontronic Maxwell's demon was added through the triboelectric-induced polarization, which generated a negative electrostatic field and thus enhanced the asymmetric EDLs. This enhancement led to significant improvements in the performance of the EP-TING (Figures 2K and S14). The $I_{SC}$ and $Q_{SC}$ of the EP-TING increased to 31.10 μA and 1.73 μC, respectively. By contrast, when a positively charged nylon (PI) film was applied on the top Au/FEP layer, the positive

**Figure 2. Adjustment of EDL charge distribution by triboelectric-induced polarization as triboiontronic Maxwell's demon**

(A) The charge density in the EDL could be adjusted by triboelectric-induced polarization.

(B–D) The regulation principle of the charge density in EDL.

(E and F) The charge density in the EDL could be increased by increasing the electronegativity of dielectric materials.

(G and H) By reducing the sputtering time of metal layers on dielectric substrates, the charge density in EDLs at hybrid film-water interfaces could be increased.

(I) The effect of metal layer sputtering time on the device's internal resistance.

(J) The effect of metal layer sputtering time on the output of conventional TINGs without the influence of triboelectric-induced polarization.

(K) The effect of triboelectric-induced polarization on the EP-TING output.

(L–O) Comparison of charge distributions in asymmetric EDLs constructed by different solid material-water upon contacts.

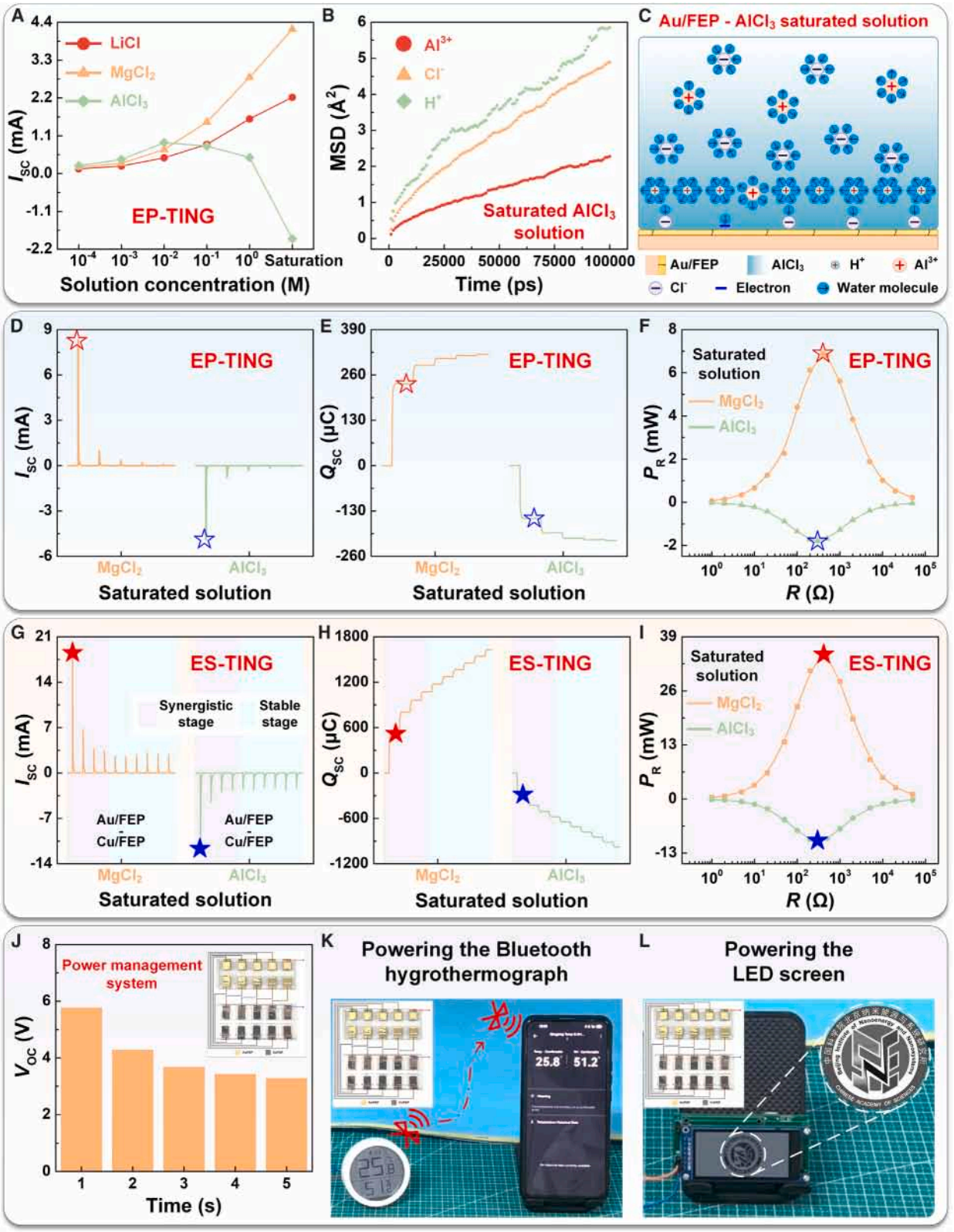


*(legend on next page)*

electrostatic field generated a reverse triboelectric-induced polarization, which weakened the $I_{SC}$ and $Q_{SC}$ to 16.47 μA and 1.07 μC, respectively. Thus, the integration of triboelectric-induced polarization-based triboiontronic Maxwell's demon with the Au/FEP hybrid material enabled the EP-TING to achieve efficient ion migration via enhanced asymmetric EDLs, establishing a strong foundation for seamless energy-information flow. Based on the dynamic regulation of the EDLs described above, the charge distributions in asymmetric EDLs formed by various solid-liquid interfaces were compared. The EDL at the dielectric-liquid interface exhibited a higher charge density (Figure 2L), which enhanced the ion concentration gradient between the asymmetric EDLs and improved cation migration efficiency. However, the insulating properties of the dielectric limited the conversion of ion migration into electron transfer within the external circuit, leading to an $I_{SC}$ of 0 μA for this system. By contrast, pure Au demonstrated excellent electrical conductivity. The EDL at the Au-liquid interface had a significantly lower charge density compared with the dielectric-liquid interface, with an opposite charge distribution due to a difference in electronegativity, resulting in a weaker ion concentration gradient across the asymmetric EDLs (Figure 2M). It led to a weaker migration of anions as charge carriers, resulting in an $I_{SC}$ of only around −0.8 μA (Figure S15). To overcome this limitation, asymmetric EDLs should be constructed using the metal/dielectric hybrid film in contact with the liquid (Figure 2N). By fine-tuning the dielectric's electronegativity, it was possible to precisely modulate the solid-liquid CE to create an effective ion concentration gradient that facilitated ion migration. Meanwhile, the ultrathin metal layer served as a charge-collecting layer, converting ion migration into electron transfer. This configuration led to an increase in $I_{SC}$ to 23.57 μA in conventional TING without the influence of triboelectric-induced polarization. Furthermore, the application of a negative electrostatic field to the FEP surface in the top Au/FEP hybrid film, via solid-solid CE, leveraged the triboiontronic Maxwell's demon created by triboelectric-induced polarization, resulting in further enhancement of the asymmetric EDLs. This promoted a more pronounced ion concentration gradient (Figure 2O), ultimately increasing the $I_{SC}$ to 31.10 μA in the ES-TING. To improve the long-term stability of triboelectric-induced polarization and ensure sustained functionality in triboiontronic applications, several strategies could be implemented. Firstly, surface engineering techniques, such as structured doping of ferroelectric inorganic nanoparticles to create charge traps[46] or the design of nano/microstructured dielectric surfaces, could be employed to enhance charge retention and establish a robust electret-based strategy for improved long-term polarization stability. Secondly, environmental control, such as encapsulating the device with hydrophobic coatings or operating under low-humidity conditions, could effectively minimize charge loss by limiting interactions with water molecules and other charge-neutralizing species. Thirdly, active charge replenishment strategies, including periodic triboelectric activation or electrostatic pre-charging, could help counteract charge dissipation and maintain a stable electrostatic field over extended periods.

## Harnessing triboiontronic Maxwell's demon for efficient energy flow

After optimizing the solid phase, a systematic study of the charge-carrying capacity of ions in the liquid phase was essential to significantly enhance the EP-TING output. As shown in Figure 3A, increasing the LiCl concentration from $10^{-4}$ M to saturation led to a substantial rise in the $I_{SC}$ of the EP-TING from 0.14 to 2.22 mA, which could be attributed to two primary factors. Firstly, a higher ion concentration increased the charge density in the bottom EDL, amplifying the asymmetry of the EDLs. Secondly, the increased ion concentration improved the solution's conductivity, reducing the device's internal resistance from approximately 6 kΩ to 500 Ω. Additionally, replacing $Li^+$ with $Mg^{2+}$ at the same concentration significantly enhanced the output, with saturated $MgCl_2$ as the liquid phase, enabling the EP-TING to achieve an $I_{SC}$ of 4.22 mA. This enhancement highlighted the influence of higher valence states on ion charge-carrying capacity, enabling more efficient current output at equivalent cation concentrations. However, when using $Al^{3+}$ ions as the charge carrier, a different ion kinetic behavior was observed. Although the EP-TING with $AlCl_3$ showed superior performance compared with LiCl and $MgCl_2$ at concentrations below $10^{-2}$ M, its output declined as the concentration further increased. Notably, with the saturated $AlCl_3$ solution, the EP-TING even produced a negative $I_{SC}$ of −1.90 mA (the corresponding $Q_{SC}$ values in this experiment are shown in Figures S16–S18). Due to the hydrolysis of the saturated $AlCl_3$ solution, which produced $Al(OH)_3$ and released $H^+$ ions, its pH value was approximately 0.1 (Figure S19), indicating a significantly higher concentration of $H^+$ compared with LiCl and $MgCl_2$ solutions. MD simulations on the saturated $AlCl_3$ solution were conducted, and mean squared displacement (MSD) curves for various ions in the solution were analyzed (Figure 3B). The simulation results showed that the diffusion coefficients follow the order of $H^+ > Cl^- > Al^{3+}$, which could be explained by the different sizes, charges, and hydration behaviors of the ions. $H^+$ exhibited the highest diffusion coefficient due to its small size and the Grotthuss mechanism, where protons effectively "hop" between water molecules. $Cl^-$, being a monovalent ion, had a larger radius than $H^+$ but still moved relatively freely due to its lower charge density. $Al^{3+}$, as a highly charged trivalent ion, formed a strongly hydrated complex,

**Figure 3. Harnessing triboiontronic Maxwell's demon for efficient energy flow**

(A) The effect of ion's charge-carrying capacity on the EP-TING output.

(B) MD simulations on the high-concentration $AlCl_3$ solution were conducted.

(C) The EDL model at the contact interface between Au/FEP hybrid film and saturated $AlCl_3$ solution.

(D–F) The optimal output generated by the EP-TING with different saturated solutions under the action of triboiontronic Maxwell's demon.

(G–I) The optimal output generated by the ES-TING with different saturated solutions under the action of triboiontronic Maxwell's demon.

(J) The $V_{OC}$ of the power management system could reach 6 V.

(K and L) The power management system could power a Bluetooth thermometer and an LED screen.

which significantly increased its effective radius and reduced its mobility. This resulted in its lowest diffusion coefficient among the three ions. The MSD results correlated with these physical properties and likely provided an accurate representation of ion diffusion behavior in the higher-concentration solution. Upon contact between the Au/FEP hybrid film and the $AlCl_3$ solution, $H^+$ swiftly migrated to the interface, forming the OHP within the Stern layer (Figure 3C). Simultaneously, the IHP was occupied by $Cl^-$ and electrons transferred via CE, while the majority of $Cl^-$ functioned as charge carriers, resulting in a negative $I_{SC}$. Particularly, the EP-TING with saturated $AlCl_3$ required triboiontronic Maxwell's demon to apply a positive electrostatic field on the back of the top Au/PET layer to promote the against concentration migration of ions and promote the generation of electrical energy (Figure S20). As a verification, when using a 1 M HCl solution as the liquid phase (Figure S21), the EP-TING also generated negative electrical signals (Figure S22). This experiment demonstrated that varying the type or concentration of ions in solutions allows the regulation of charge carriers with different polarities, thereby controlling the current direction of EP-TINGs and laying the groundwork for logical control. Moreover, to further enhance the asymmetry of two EDLs at the same solution concentration, plasma treatment was applied to modify the hydrophilicity of the bottom Au/FEP surface. As the 50 W-power plasma treatment duration increased to 40 s, the contact angle decreased significantly from approximately 93° to 23° (Figure S23), indicating a marked improvement in the hydrophilicity. This treatment could effectively increase the charge density in the bottom EDL, resulting in a stronger ion concentration gradient, ultimately leading to improved EP-TING output. Experiments demonstrated that, under the influence of a negative electrostatic field applied to the back of the top Au/PET layer through triboiontronic Maxwell's demon, the EP-TING system with saturated $MgCl_2$ exhibited enhanced electrical performance. This optimization, driven by hydrophilic adjustment, resulted in an $I_{SC}$ of 8.30 mA, $Q_{SC}$ of 234.74 μC, peak power ($P_R$) of 6.89 mW, internal resistance of 400 Ω, and open-circuit voltage ($V_{OC}$) of 0.33 V (Figures 3D–3F and S24). Conversely, under the action of a positive electrostatic field at the same position, the EP-TING with saturated $AlCl_3$ could achieve negative optimal output with the $I_{SC}$ of −4.89 mA, $Q_{SC}$ of −151.20 μC, $P_R$ of −1.79 mW, internal resistance of 300 Ω, and $V_{OC}$ of −0.28 V (Figure S25), respectively. In addition, scanning electron microscopy (SEM) imaging was conducted to examine any microstructural changes in the composite material before and after immersion in the solution (Figure S26). The imaging results demonstrated that solution exposure had no significant impact on the Au layer or the pre-existing microcracks.

To further improve the output performance and operation stability, redox reactions could be integrated into the EP-TING and transformed into a more efficient ES-TING by flexibly adjusting the type of metal sputtered on the dielectric substrate. In the EP-TING with saturated $MgCl_2$, cations were driven upward by the concentration gradient. Therefore, in the corresponding ES-TING, the bottom Au/FEP layer needed to be replaced with Cu/FEP to ensure that Cu was oxidized to $Cu^{2+}$. This allowed $Cu^{2+}$ to be driven upward by the electrochemical potential, working synergistically with other cations driven by asymmetric EDLs (Note S1; Figure S27). This redox reaction synergized with the enhanced asymmetric EDLs, facilitating the upward migration of multiple cations and creating an effective synergistic stage. This interaction significantly improved the device's operational stability, even after the dissipation of the asymmetric EDLs, transitioning the system into a stable stage. Under the action of a negative electrostatic field applied by triboiontronic Maxwell's demon, the ES-TING with saturated $MgCl_2$ could enhance the positive optimal output to the $I_{SC}$ of 18.62 mA, $Q_{SC}$ of 523.74 μC, $P_R$ of 34.67 mW, internal resistance of 400 Ω, and $V_{OC}$ of 0.60 V, respectively (Figures 3G–3I and S28). Conversely, in the EP-TING with saturated $AlCl_3$, anions migrated upward as charge carriers. The top Au/FEP needed to be replaced by Cu/FEP in the ES-TING, which ensured that the ion concentration gradient promoted upward anion migration while the redox reaction drove $Cu^{2+}$ ions downward, thereby producing a synergistic net current output during the synergistic stage (Figure S29). Under the action of a positive electrostatic field applied by triboiontronic Maxwell's demon, the ES-TING with saturated $AlCl_3$ could generate the negative optimal with the $I_{SC}$ of −11.63 mA, $Q_{SC}$ of −289.17 μC, $P_R$ of −10.14 mW, internal resistance of 300 Ω, and $V_{OC}$ of −0.58 V (Figure S30), respectively. After calculation, the transferred charge density of the EP-TING and ES-TING could reach 2,347.12 and 5,237.51 mC/m$^2$, respectively (Figure 1H), which were increased by several orders of magnitude compared with conventional TENGs, TINGs, and other EDL-regulated energy-harvesting technologies. The EP-TING operated exclusively through the enhanced formation of the asymmetric EDLs. After the operation, the symmetric EDL state could be easily restored to its initial asymmetric state through a simple electrochemical recovery process (Figures S31 and S32), ensuring excellent reusability and long-term operational stability. This made the EP-TING particularly advantageous for applications requiring extended standby periods, intermittent activation, and minimal maintenance. In the ES-TING, the synergy between the redox reaction and asymmetric EDL formation enhanced energy conversion efficiency, so it was ideal for environments requiring sustained high-energy supply, such as powering high-demand sensors or enabling long-duration underwater wireless communication. To enhance the direct energy supply to load devices and minimize energy loss, 10 ES-TINGs were connected in series to form a power management system (Figure S33). This setup enabled the direct integration of the energy-harvesting device that dynamically adjusts the EDL with the energy storage device through redox reactions, eliminating the need for complex energy conversion circuits (Figure S34). This configuration increased the $V_{OC}$ to approximately 6 V (Figures 3J and S35), facilitating the direct operation of electronic devices. For instance, the power management system could charge a 1 mF capacitor to around 3 V in 25 s (Figure S36). During the synergistic stage, the charging process was notably efficient, while the stable stage maintained consistent charging stability. In practical applications, the power management system demonstrated its capability to power a Bluetooth thermometer, enabling wireless environmental information transmission to a mobile device via Bluetooth (Figures 3K and S37; Video S1), and to power an light emitting diode (LED) screen for displaying essential information (Figures 3L and S38; Video S2). These

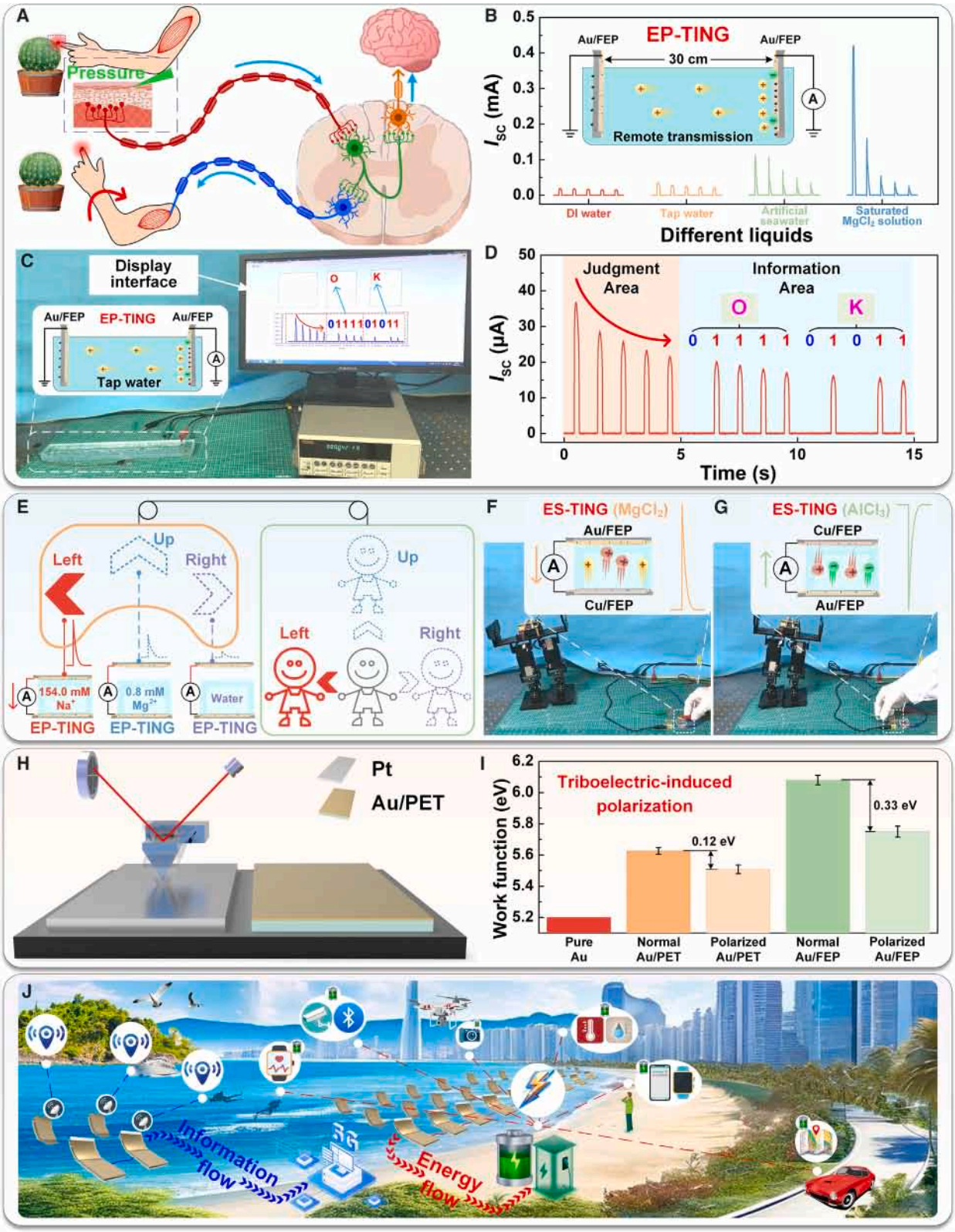


*(legend on next page)*

examples highlighted the ES-TING's practical value as a reliable energy source and underscored its promising potential as an efficient power unit for future Internet of Things (IoT) applications. According to the stability test, it was observed that a Cu layer, with a thickness of tens of nanometers, sputtered onto the FEP substrate, could maintain stable operation of the ES-TING device for nearly 2 h (Figure S39). To mitigate the degradation of the Cu charge-collecting layer due to the redox reaction and extend the operational lifespan of the ES-TING, several strategies could be applied. Firstly, appropriately increasing the thickness of the Cu layer could significantly enhance the device's durability. Secondly, due to the relatively low cost of Cu, periodic replacement of the Cu/FEP hybrid film could be a cost-effective strategy. Finally, optimizing cycling parameters, such as amplitude and frequency, could help reduce metal degradation by controlling the rate of cycling-induced stress.

## Harnessing triboiontronic Maxwell's demon for efficient information flow

The transmission distance of neural signals in the human body varies depending on the type and function of specific nerve fibers, ranging from a few millimeters to about a meter. In pain reflex circuits (Figure 4A), the sodium-potassium pump functions similarly to a biological Maxwell's demon, efficiently converting ATP into electrochemical energy to maintain ion gradients essential for sustaining the effective propagation of sensory signals and motor commands between sensory and motor neurons. This active regulation enables signal transmission over distances typically spanning several to tens of centimeters, ensuring rapid and efficient communication within the nervous system. Analogously, in the EP-TING, the triboiontronic Maxwell's demon plays a critical role in optimizing the effective range of remote ion migration with minimal energy consumption. By fine-tuning the spatial configuration of the two Au/FEP-liquid interfaces, the interaction distance of the enhanced asymmetric EDLs, regulated by the triboiontronic Maxwell's demon, could be adjusted within the EP-TING. The asymmetric EDLs significantly expanded the effective range of ionic-electronic coupling beyond the nanoscale of the EDL itself and even extended it several orders of magnitude higher than that achieved by a single EDL, reaching tens of centimeters. This dynamic control enabled the bionic circuit to maintain stable operation across a variety of liquid environments, including electrolyte solutions (e.g., saturated $MgCl_2$), artificial seawater (0.6 M NaCl), tap water, and deionized (DI) water (Figures 4B and S40). Remarkably, the bionic circuit, with a compact working area of just 1 $cm^2$, maintained effective performance across various liquid phases, achieving interaction distances of up to 30 cm. This was comparable to neural transmission distances and generated $I_{SC}$ values of 420, 110, 40, and 20 μA, respectively. This robust remote signal transmission capability provided a solid foundation for bionic circuits to transmit mechanically encoded physical contact information over longer distances, converting it into corresponding electrical signals (Figures 1I and 4C). These encoded electrical signals are subsequently collected and translated into readable character information using the ASCII system (Figure 4D; Video S3). To minimize information distortion caused by chaotic pulses in ambient noise, a judgment area was established, encompassing signals that consistently decreased during the initial five contact-separation cycles. This approach could effectively identify the information source and be regenerated. Following numerous cycles of information transmission, an external electrical field could be employed to recover the mechanical-driven electrode, restoring the enhanced asymmetric EDL for subsequent transmissions (Figure S41). To further stabilize wireless information transmission, redox reactions could be incorporated to create a bionic neurological circuit via the ES-TING (Note S2; Figure S42). This circuit effectively controlled ion migration by synergizing enhanced asymmetric EDLs with redox reactions, thereby increasing the $I_{SC}$ amplitude for improved signal recognition (Figure S43) and ensuring reliable information transmission (Figure S44; Video S4). However, relying solely on redox reactions might impair information identification due to the absence of the judgment area, leading to interference from environmental pulses and erroneous transmission (Figure S45; Video S5). For demonstration purposes, the character information of OK via the ASCII system was successfully conveyed through electrical pulses generated by the corresponding mechanical actions. Therefore, integrating triboiontronic Maxwell's demon to enhance asymmetric EDLs was crucial for precise wireless communication. Calculations showed that the quality factor *Q* of the bionic neurological circuit via the EP-TING and ES-TING is 12.0 and 23.1 A/m, respectively (Figure 1J), substantially higher than the approximately 5 A/m observed in conventional TENGs.[38–43] Therefore, utilizing triboiontronic Maxwell's demon through enhanced asymmetric EDLs significantly could enhance the signal-to-noise ratio and improve the accuracy of information source identification, thereby enhancing anti-interference capabilities in wireless information transmission. This approach successfully mitigated the limitations of existing underwater communication methods, where electromagnetic waves are absorbed by water, optical communication is disrupted by ambient light, and widely adopted acoustic communication is compromised by multipath interference and Doppler shift. Additionally,

**Figure 4. Harnessing triboiontronic Maxwell's demon for efficient information flow**

(A) Action potential transfer process in human pain reflex circuit.

(B) The bionic neurologic circuit via EP-TING could control the remote migration of ions.

(C) The bionic neurologic circuit could realize the remote wireless transmission of complex information underwater.

(D) Using the ASCII system, encoded electronic pulses could be translated into readable characters.

(E) A human-computer interaction interface was developed by the bionic neural control system via EP-TINGs.

(F and G) By using the human-computer interaction interface, the flexible control of intelligent devices such as robots could be realized.

(H) The test system for measuring metal work function by the KPFM.

(I) The metal work function could be adjusted by triboelectric-induced polarization.

(J) EP-TINGs and ES-TINGs have a potentially wide range of applications in the IoT.

in comparison to conventional TENGs, the bionic circuit could not only deliver superior information recognition but also achieve extended transmission distances with a minimal working area of 1 $cm^2$, thereby advancing the device's miniaturization and portability.

Building on the principles of efficient energy-information transmission, the nervous system leverages parallel processing and specialized transmission pathways to manage multiple signals simultaneously. This ensures precise and coordinated functioning throughout the body. For example, in the pain reflex circuit (Figure 4A), sensory receptors detect stimuli and generate action potentials that travel along sensory neurons to the central nervous system. Concurrently, the central nervous system processes these signals in parallel, issuing motor commands through motor neurons to induce muscle responses and avoid injury, while also relaying memory-related information to the brain through memory neurons to inform future behavior. Inspired by these processes, a bionic neural control system was developed by integrating multiple bionic neurological circuits using EP-TINGs with solutions of varying concentrations, mimicking the parallel processing and specialized transmission capabilities of the biological nervous system. This setup enabled the creation of a human-computer interaction interface that operates based on multiple threshold activations (Figure S46). By replicating ion concentrations similar to those in the human body, utilizing 154 mM NaCl, 0.8 mM $MgCl_2$, and DI water as the liquid phases in EP-TINGs, distinct signal amplitudes (2.00, 0.41, and 0.14 mA) were generated (Figure S47). When different bionic circuits in the bionic neural control system were activated by the user through the interface, specific signal amplitudes triggered corresponding movements in a virtual human displayed on the computer interface (Figure 4E; Video S6). Additionally, by adjusting the opposing currents from different ion types within the ES-TING liquid phase (Figure S48), a stable bionic neural control system was developed (Figure S49), which served as a reliable human-computer interaction interface to control intelligent devices to perform desired functions. Taking the example of controlling the robot to perform the rhythmic walking motion (Video S7), when the ES-TING with a saturated $MgCl_2$ generated a positive signal, it prompted the robot to lift its right leg (Figure 4F). Conversely, a negative signal from the ES-TING with a saturated $AlCl_3$ solution caused the robot to lift its left leg (Figure 4G). Leveraging the triboiontronic Maxwell's demon via triboelectric-induced polarization, efficient wireless information transmission underwater and a flexible, energy-independent human-computer interface were achieved, seamlessly integrating energy harvesting, sensing, storage, and computing. Additionally, dynamic fine-tuning of the metal work function could be enabled by triboiontronic Maxwell's demon. By using stable platinum (Pt) with a work function of 5.65 eV as a reference, the surface potential difference between Pt and the test sample was measured using a Kelvin probe force microscope (KPFM) to assess the work function (Figure 4H). Compared with the 5.20 eV work function of pure Au, the work functions of Au sputtered onto PET and FEP (10 min of sputtering) increased to 5.63 and 6.08 eV, respectively (Figures 4I, S50, and S51). This observation indicated that the CE between the Au layer and the dielectric substrate facilitated electron transfer from the Au surface to the contact interface, thereby lowering the tendency for electron escape from the metal surface. Conversely, when the back surfaces of these hybrid films were rubbed with fur, introducing additional electrons via solid-solid CE, the work functions dropped to approximately 5.51 and 5.75 eV, respectively (Figures 4I, S52, and S53). This research demonstrated that triboelectric-induced polarization, functioning as triboiontronic Maxwell's demon, generates an electrostatic field by utilizing triboelectric energy, facilitating electron transfer from the Au layer to the surface, and enabling dynamic modulation of the metal work function through the redistribution of electrons. It extends beyond iontronic applications, providing transformative potential for optimizing interfacial contact potentials in perovskite photovoltaics and advancing broader technological domains. Additionally, triboiontronics enhances energy and information flow, ensuring optimal energy transmission, storage, and utilization. It also improves information transfer efficiency, reduces energy consumption and latency, and enhances the responsiveness and stability of IoT devices (Figure 4J). These advancements, driven by the concept of triboiontronic Maxwell's demon, offer substantial promise for the future of intelligent interconnectivity.

## Conclusions

In summary, a triboiontronic Maxwell's demon was established in this paper through triboelectric-induced polarization of electrostatic fields. This approach facilitates remote regulation of charge distribution and migration within EDLs while enabling fine-tuning of metal work functions, thereby offering versatile control over energy and information flow. The enhanced EP-TING demonstrated a substantial charge transfer density of 2,347.12 $mC/m^2$, marking a significant advancement over traditional EDL-based energy-harvesting technologies. Further enhancements were realized with the ES-TING, where integrated redox reactions boosted the transferred charge density to 5,237.51 $mC/m^2$, establishing it as a stable, efficient power management unit. By constructing asymmetric EDLs, the system not only optimized high-energy flows but also achieved high-fidelity underwater information transmission. Bionic neural circuits built with EP-TINGs or ES-TINGs enabled portable, remote, interference-resistant wireless communication with minimal energy consumption in aqueous environments, effectively mirroring the efficiency of neural signal transmission. This approach addresses major challenges such as rapid electromagnetic wave absorption in water, optical communication's vulnerability to ambient light interference, and acoustic communication limitations caused by multipath interference and Doppler effects. Furthermore, by leveraging ion modulation within bionic neural circuits using EP-TINGs or ES-TINGs, precise control over charge carrier polarity and current direction has been achieved, paving the way for energy-autonomous human-machine interfaces and advanced logic control systems. Additionally, triboelectric-induced polarization offers dynamic tuning of metal work functions, significantly enhancing energy conversion efficiencies in perovskite photovoltaics and other applications. Overall, this work establishes a solid foundation for energy-efficient, multi-signal processing IoT systems, advancing the development of intelligent, interconnected technologies in the post-Moore era.

## METHODS

### Materials

The ultrathin metal layers on the dielectric substrate surfaces in the hybrid material were deposited using a magnetron sputtering system (Discovery 635, Denton Vacuum, USA). The sputtering process was carried out with a power of 50 W, and the substrate rotation speed was maintained at 40 rpm to ensure uniform deposition. After the sputtering process, the resulting thickness of the ultrathin metal layer was approximately 100 nm.

### Fabrication of the EP-TING and ES-TING

The EP-TING and ES-TING devices, each with an area of 1 $cm^2$, were constructed using PET, PI, PTFE, and FEP film substrates, all with a thickness of 100 μm. The bottom hybrid material surface underwent plasma treatment using a plasma cleaner (CPC-A, CIF, China) for 30 s to enhance surface hydrophilicity.

### Electrical measurement

The EP-TING and ES-TING devices were driven by a linear motor (PL0119x600/520, LinMot, Switzerland) for normal operation. Their output electrical signals were measured using a test system composed of an electrometer (6514, Keithley, USA) and a data acquisition card (BNC-2120, National Instruments, USA). A Faraday cylinder was employed to test the charge on droplets sliding over the film, while a high-speed surface potentiometer (347, TREK, USA) measured the film's surface potential. The KPFM measurement was conducted on an atomic force microscope (Cypher ES, Oxford, UK) using a conductive probe (NSC 18, MikroMash, USA). The tapping amplitude was set to 350 mV, with a scan size of 1 μm and a lift height of 50 nm for precise surface potential analysis.

## RESOURCE AVAILABILITY

### Lead contact

Further information and requests for resources and reagents should be directed to and will be fulfilled by the lead contact, Di Wei (dw344@cam.ac.uk).

### Materials availability

The materials generated in this study are available from the lead contact upon reasonable request.

### Data and code availability

The data used to support the findings of this study are available from the lead contact upon reasonable request.

## ACKNOWLEDGMENTS

This work was supported by the National Natural Science Foundation (grant no. 22479016).

## AUTHOR CONTRIBUTIONS

D.W. and Z.L.W. conceptualized the idea and led the project. D.W. was responsible for designing the experiments and overseeing the entire project. X.L. conducted the primary experiments and performed the data analysis. KPFM measurements were carried out by X.L. and Y.W., while X.G. and Z.Z. handled the MD simulations. All authors contributed to discussions of the results and provided feedback on the manuscript. The paper was written by D.W. and X.L.

## DECLARATION OF INTERESTS

The authors declare no competing interests.

## SUPPLEMENTAL INFORMATION

Supplemental information can be found online at https://doi.org/10.1016/j.joule.2025.101888.

Received: November 5, 2024
Revised: February 12, 2025
Accepted: March 7, 2025
Published: March 31, 2025

## REFERENCES

1. Maxwell, J.C. (1892). Theory of Heat. Nature *45*, 222. https://doi.org/10.1038/045222c0.
2. Ribezzi-Crivellari, M., and Ritort, F. (2019). Large work extraction and the Landauer limit in a continuous Maxwell demon. Nat. Phys. *15*, 660–664. https://doi.org/10.1038/s41567-019-0481-0.
3. Koski, J.V., Maisi, V.F., Sagawa, T., and Pekola, J.P. (2014). Experimental observation of the role of mutual information in the nonequilibrium dynamics of a Maxwell demon. Phys. Rev. Lett. *113*, 030601. https://doi.org/10.1103/PhysRevLett.113.030601.
4. Raizen, M.G. (2009). Comprehensive control of atomic motion. Science *324*, 1403–1406. https://doi.org/10.1126/science.1171506.
5. Brillouin, L. (1951). Maxwell's Demon Cannot Operate: Information and Entropy. I. J. Appl. Phys. *22*, 334–337. https://doi.org/10.1063/1.1699951.
6. Barredo, D., de Léséleuc, S., Lienhard, V., Lahaye, T., and Browaeys, A. (2016). An atom-by-atom assembler of defect-free arbitrary two-dimensional atomic arrays. Science *354*, 1021–1023. https://doi.org/10.1126/science.aah3778.
7. Endres, M., Bernien, H., Keesling, A., Levine, H., Anschuetz, E.R., Krajenbrink, A., Senko, C., Vuletic, V., Greiner, M., and Lukin, M.D. (2016). Atom-by-atom assembly of defect-free one-dimensional cold atom arrays. Science *354*, 1024–1027. https://doi.org/10.1126/science.aah3752.
8. Chu, S. (1991). Laser manipulation of atoms and particles. Science *253*, 861–866. https://doi.org/10.1126/science.253.5022.861.
9. Kumar, A., Wu, T.-Y., Giraldo, F., and Weiss, D.S. (2018). Sorting ultracold atoms in a three-dimensional optical lattice in a realization of Maxwell's demon. Nature *561*, 83–87. https://doi.org/10.1038/s41586-018-0458-7.
10. Cottet, N., Jezouin, S., Bretheau, L., Campagne-Ibarcq, P., Ficheux, Q., Anders, J., Auffèves, A., Azouit, R., Rouchon, P., and Huard, B. (2017). Observing a quantum Maxwell demon at work. Proc. Natl. Acad. Sci. USA *114*, 7561–7564. https://doi.org/10.1073/pnas.1704827114.
11. Xie, X., Crespo, G.A., Mistlberger, G., and Bakker, E. (2014). Photocurrent generation based on a light-driven proton pump in an artificial liquid membrane. Nat. Chem. *6*, 202–207. https://doi.org/10.1038/nchem.1858.
12. Pruchyathamkorn, J., Nguyen, B.T., Grommet, A.B., Novoveska, M., Ronson, T.K., Thoburn, J.D., and Nitschke, J.R. (2024). Harnessing Maxwell's demon to establish a macroscale concentration gradient. Nat. Chem. *16*, 1558–1564. https://doi.org/10.1038/s41557-024-01549-2.
13. Zimmermann, K., Leffler, A., Babes, A., Cendan, C.M., Carr, R.W., Kobayashi, J., Nau, C., Wood, J.N., and Reeh, P.W. (2007). Sensory neuron sodium channel $Na_V1.8$ is essential for pain at low temperatures. Nature *447*, 855–858. https://doi.org/10.1038/nature05880.
14. Branco, T., Tozer, A., Magnus, C.J., Sugino, K., Tanaka, S., Lee, A.K., Wood, J.N., and Sternson, S.M. (2016). Near-Perfect Synaptic Integration by NaV1.7 in Hypothalamic Neurons Regulates Body Weight. Cell *165*, 1749–1761. https://doi.org/10.1016/j.cell.2016.05.019.
15. Müller, C., and Remy, S. (2016). Slowly Building Excitement. Cell *165*, 1568–1569. https://doi.org/10.1016/j.cell.2016.06.005.

16. Morth, J.P., Pedersen, B.P., Toustrup-Jensen, M.S., Sørensen, T.L.M., Petersen, J., Andersen, J.P., Vilsen, B., and Nissen, P. (2007). Crystal structure of the sodium-potassium pump. Nature *450*, 1043–1049. https://doi.org/10.1038/nature06419.

17. Kernan, R.P. (1962). Membrane potential changes during sodium transport in frog sartorius muscle. Nature *193*, 986–987. https://doi.org/10.1038/193986a0.

18. Sarpeshkar, R. (1998). Analog versus digital: extrapolating from electronics to neurobiology. Neural Comput. *10*, 1601–1638. https://doi.org/10.1162/089976698300017052.

19. Qian, H., Wei, D., and Wang, Z. (2023). Bionic iontronics based on nanoconfined structures. Nano Res. *16*, 11718–11730. https://doi.org/10.1007/s12274-023-5705-z.

20. Yang, L., Li, S., Qian, H., Wang, Z., Wang, Z.L., and Wei, D. (2024). Osmotic power generation based on nanoconfined materials. MRS Energy Sustain. *11*, 193–218. https://doi.org/10.1557/s43581-024-00104-3.

21. Yang, L., Yang, F., Liu, X., Li, K., Zhou, Y., Wang, Y., Yu, T., Zhong, M., Xu, X., Zhang, L., et al. (2021). A moisture-enabled fully printable power source inspired by electric eels. Proc. Natl. Acad. Sci. USA *118*, e2023164118. https://doi.org/10.1073/pnas.2023164118.

22. Qian, H., Peng, P., Fan, H., Yang, Z., Yang, L., Zhou, Y., Tan, D., Yang, F., Willatzen, M., Amaratunga, G., et al. (2024). Horizontal Transport in Ti3C2Tx MXene for Highly Efficient Osmotic Energy Conversion from Saline-Alkali Environments. Angew. Chem. Int. Ed. Engl. *63*, e202414984. https://doi.org/10.1002/anie.202414984.

23. Yang, F., Peng, P., Yan, Z.-Y., Fan, H., Li, X., Li, S., Liu, H., Ren, T.-L., Zhou, Y., Wang, Z.L., and Wei, D. (2024). Vertical iontronic energy storage based on osmotic effects and electrode redox reactions. Nat. Energy *9*, 263–271. https://doi.org/10.1038/s41560-023-01431-4.

24. Li, X., Li, S., Guo, X., Shao, J., Wang, Z.L., and Wei, D. (2023). Triboiontronics for efficient energy and information flow. Matter *6*, 3912–3926. https://doi.org/10.1016/j.matt.2023.08.022.

25. Li, X., Wang, Z.L., and Wei, D. (2024). Scavenging Energy and Information through Dynamically Regulating the Electrical Double Layer. Adv. Funct. Materials *34*, 2405520. https://doi.org/10.1002/adfm.202405520.

26. Wei, D., Yang, F., Jiang, Z., and Wang, Z. (2022). Flexible iontronics based on 2D nanofluidic material. Nat. Commun. *13*, 4965. https://doi.org/10.1038/s41467-022-32699-x.

27. Peng, P., Qian, H., Liu, J., Wang, Z., and Wei, D. (2024). Bioinspired ionic control for energy and information flow. Int. J. Smart Nano Mater. *15*, 198–221. https://doi.org/10.1080/19475411.2024.2305393.

28. Li, X., Li, R., Li, S., Wang, Z.L., and Wei, D. (2024). Triboiontronics with temporal control of electrical double layer formation. Nat. Commun. *15*, 6182. https://doi.org/10.1038/s41467-024-50518-3.

29. Zhang, H.L., Wang, K.Q., Li, J.J., Li, J.F., Zhang, R., and Zheng, Y.L. (2022). Liquid-based nanogenerator fabricated by a self-assembled fluoroalkyl monolayer with high charge density for energy harvesting. Matter *5*, 1466–1480. https://doi.org/10.1016/j.matt.2022.02.013.

30. He, W.C., Shan, C.C., Fu, S.K., Wu, H.Y., Wang, J., Mu, Q.J., Li, G., and Hu, C.G. (2023). Large harvested energy by self-excited liquid suspension triboelectric nanogenerator with optimized charge transportation behavior. Adv. Mater. *35*, e2209657. https://doi.org/10.1002/adma.202209657.

31. Yang, C.J., Wang, Y.M., Wang, Y., Zhao, Z.H., Zhang, L.W., and Chen, H.W. (2023). Highly stretchable PTFE particle enhanced triboelectric nanogenerator for droplet energy harvestings. Nano Energy *118*, 109000. https://doi.org/10.1016/j.nanoen.2023.109000.

32. Cheng, B.L., Qi, C.X., Ding, Y.Q., Jia, X.F., Bai, S., Xu, Q., Yu, Y.D.C., Wen, J., and Qin, Y. (2023). High output performance flutter-driven triboelectric nanogenerator. Nano Energy *106*, 108106. https://doi.org/10.1016/j.nanoen.2022.108106.

33. Wang, Z.Z., Zhang, Z., Chen, Y.K., Gong, L.K., Dong, S.C., Zhou, H., Lin, Y., Lv, Y., Liu, G.X., and Zhang, C. (2022). Achieving an ultrahigh direct-current voltage of 130 V by semiconductor heterojunction power generation based on the tribovoltaic effect. Energy Environ. Sci. *15*, 2366–2373. https://doi.org/10.1039/d2ee00180b.

34. Qiao, W., Zhao, Z., Zhou, L., Liu, D., Li, S., Yang, P., Li, X., Liu, J., Wang, J., and Wang, Z.L. (2022). Simultaneously enhancing direct-current density and lifetime of tribovotaic nanogenerator via interface lubrication. Adv. Funct. Materials *32*, 2208544. https://doi.org/10.1002/adfm.202208544.

35. Xue, G., Xu, Y., Ding, T., Li, J., Yin, J., Fei, W., Cao, Y., Yu, J., Yuan, L., Gong, L., et al. (2017). Water-evaporation-induced electricity with nanostructured carbon materials. Nat. Nanotechnol. *12*, 317–321. https://doi.org/10.1038/nnano.2016.300.

36. Yin, J., Li, X.M., Yu, J., Zhang, Z.H., Zhou, J.X., and Guo, W.L. (2014). Generating electricity by moving a droplet of ionic liquid along graphene. Nat. Nanotechnol. *9*, 378–383. https://doi.org/10.1038/Nnano.2014.56.

37. Yin, J., Zhang, Z., Li, X., Yu, J., Zhou, J., Chen, Y., and Guo, W. (2014). Waving potential in graphene. Nat. Commun. *5*, 3582. https://doi.org/10.1038/ncomms4582.

38. Zhao, H., Xu, M., Shu, M., An, J., Ding, W., Liu, X., Wang, S., Zhao, C., Yu, H., Wang, H., et al. (2022). Underwater wireless communication via TENG-generated Maxwell's displacement current. Nat. Commun. *13*, 3325. https://doi.org/10.1038/s41467-022-31042-8.

39. Feng, Y., Benassi, E., Zhang, L., Li, X., Wang, D., Zhou, F., and Liu, W. (2021). Concealed Wireless Warning Sensor Based on Triboelectrification and Human-Plant Interactive Induction. Research *2021*, 9870936. https://doi.org/10.34133/2021/9870936.

40. Das, N.K., Ravipati, M., and Badhulika, S. (2023). Nickel Metal-Organic Framework/PVDF Composite Nanofibers-based Self-Powered Wireless Sensor for Pulse Monitoring of Underwater Divers via Triboelectrically Generated Maxwell's Displacement Current. Adv. Funct. Materials *33*, 2303288. https://doi.org/10.1002/adfm.202303288.

41. Zhao, X., Zhang, D., Xu, S., Qian, W., Han, W., and Yang, Y. (2020). Self-Powered Wireless Monitoring of Obstacle Position and State in Gas Pipe via Flow-Driven Triboelectric Nanogenerators. Adv. Materials Technologies *5*, 2000466. https://doi.org/10.1002/admt.202000466.

42. Zeng, Y., Cheng, Y., Zhu, J., Jie, Y., Ma, P., Lu, H., Cao, X., and Wang, Z.L. (2022). Self-powered sensors driven by Maxwell's displacement current wirelessly provided by TENG. Appl. Mater. Today *27*, 101375. https://doi.org/10.1016/j.apmt.2022.101375.

43. Wu, N., Jiang, H., Li, W., Lin, S., Zhong, J., Yuan, F., Huang, L., Hu, B., and Zhou, J. (2017). Output enhanced compact multilayer flexible nanogenerator for self-powered wireless remote system. J. Mater. Chem. A *5*, 12787–12792. https://doi.org/10.1039/c7ta03574h.

44. Wang, Z.L., and Wang, A.C. (2019). On the origin of contact-electrification. Mater. Today *30*, 34–51. https://doi.org/10.1016/j.mattod.2019.05.016.

45. Lin, S., Xu, L., Chi Wang, A., and Wang, Z.L. (2020). Quantifying electron-transfer in liquid-solid contact electrification and the formation of electric double-layer. Nat. Commun. *11*, 399. https://doi.org/10.1038/s41467-019-14278-9.

46. Du, Y., Shen, P., Liu, H., Zhang, Y., Jia, L., Pu, X., Yang, F., Ren, T., Chu, D., Wang, Z., and Wei, D. (2024). Multi-receptor skin with highly sensitive tele-perception somatosensory. Sci. Adv. *10*, eadp8681. https://doi.org/10.1126/sciadv.adp8681.